

Scientific Objectives of Small Carry-on Impactor (SCI) and Deployable Camera 3 Digital (DCAM3-D): Observation of an Ejecta Curtain and a Crater Formed on the Surface of Ryugu by an Artificial High-Velocity Impact

M. Arakawa¹ · K. Wada² · T. Saiki³ · T. Kadono⁴ · Y. Takagi⁵ · K. Shirai⁶ · C. Okamoto¹ · H. Yano³ · M. Hayakawa³ · S. Nakazawa⁷ · N. Hirata⁸ · M. Kobayashi² · P. Michel⁹ · M. Jutzi¹⁰ · H. Imamura⁷ · K. Ogawa¹ · N. Sakatani¹¹ · Y. Iijima³ · R. Honda¹² · K. Ishibashi² · H. Hayakawa³ · H. Sawada⁷

Received: 15 August 2015 / Accepted: 8 September 2016
© Springer Science+Business Media Dordrecht 2016

Abstract The Small Carry-on Impactor (SCI) equipped on *Hayabusa2* was developed to produce an artificial impact crater on the primitive Near-Earth Asteroid (NEA) 162173 Ryugu (Ryugu) in order to explore the asteroid subsurface material unaffected by space weathering and thermal alteration by solar radiation. An exposed fresh surface by the im-

✉ M. Arakawa
masahiko.arakawa@penguin.kobe-u.ac.jp

¹ Graduate School of Science, Kobe University, 1-1, Rokkodai-cho, Nada-ku, Kobe 657-8501, Japan

² Planetary Exploration Research Center, Chiba Institute of Technology, 2-17-1 Tsudanuma, Narashino, Chiba 275-0016, Japan

³ Institute of Space and Astronautical Science, Japan Aerospace Exploration Agency, 3-1-1, Yoshinodai, Chuo-ku, Sagamihara 252-5210, Japan

⁴ University of Occupational and Environmental Health, School of Medicine, 1-1 Iseigaoka, Yahata, Kitakyusyu 807-8555, Japan

⁵ Aichi Toho University, 3-11 Heiwagaoka, Meito-ku, Nagoya 465-8515, Japan

⁶ The Graduate University for Advanced Studies, Shonan Village, Hayama, Kanagawa 240-0193, Japan

⁷ Japan Aerospace Exploration Agency, 3-1-1, Yoshinodai, Chuo-ku, Sagamihara 252-5210, Japan

⁸ University of Aizu, Aizu-Wakamatsu City, Fukushima-ken 965-8580, Japan

⁹ UMR 7293 Lagrange/CNRS, Observatoire de la Côte d'Azur, BP 4229, 06304 Nice Cedex 4, France

¹⁰ Physics Institute, Space Research and Planetary Sciences, Center for Space and Habitability, University of Bern, Sidlerstrasse 5, 3012 Bern, Switzerland

¹¹ School of Science and Technology, Meiji University, 1-1-1 Higashi-Mita, Tama-ku, Kawasaki, 214-8571, Japan

¹² Kochi Univsesity, 2-5-1 Akebono-cho, Kochi-shi, Kochi 780-8520, Japan

pactor and/or the ejecta deposit excavated from the crater will be observed by remote sensing instruments, and a subsurface fresh sample of the asteroid will be collected there. The SCI impact experiment will be observed by a Deployable CAMera 3-D (DCAM3-D) at a distance of ~ 1 km from the impact point, and the time evolution of the ejecta curtain will be observed by this camera to confirm the impact point on the asteroid surface. As a result of the observation of the ejecta curtain by DCAM3-D and the crater morphology by onboard cameras, the subsurface structure and the physical properties of the constituting materials will be derived from crater scaling laws. Moreover, the SCI experiment on Ryugu gives us a precious opportunity to clarify effects of microgravity on the cratering process and to validate numerical simulations and models of the cratering process.

Keywords Impact crater · Ejecta curtain · Crater scaling laws · Asteroid · Microgravity

1 Introduction

The main purpose of *Hayabusa2* mission is to return the sample from a primitive Near-Earth Asteroid (NEA) surface by using the sampler system on board the first *Hayabusa* mission (Tsuda et al. 2013; Tachibana et al. 2014). The target asteroid, 162173 Ryugu (Ryugu), is a C-type asteroid, and it is expected to contain organic materials in the subsurface layers, but the outermost layer of the asteroid is likely to be irradiated not only by cosmic rays but also the solar wind. Furthermore, the solar radiation at the perihelion might heat the surface (Michel and Delbo 2010) and alter its chemical composition. Thus, fresh organic materials may not be present at the asteroid surface due to these alterations and may rather be found in the subsurface. Therefore, *Hayabusa2* carries a Small Carry-on Impactor, which is called SCI in short, in order to expose fresh material from the subsurface by artificially making an impact crater. This is a very new system for asteroid explorations to support the sample science, that is, a sample unaltered by space weathering will be acquired by the sampling system through this SCI operation.

As a result of the SCI impact, which involves a 2 kg copper projectile and an impact speed of 2 km/s, an impact crater will be formed on the asteroid and a large amount of debris from the excavated crater will be ejected to form an ejecta curtain as well as the crater rim. The resulting artificial impact crater will allow revealing fresh material from the subsurface unaltered by space weathering, which will be observed by several remote sensing devices such as an Optical Navigation Camera (ONC), a Thermal InfraRed camera (TIR), a Near Infrared Spectrometer 3 (NIRS3), and a Light Detection And Ranging (LIDAR). SCI is a quite powerful method to explore the subsurface of the asteroid not only for sampling but also for remote sensing. Furthermore, it is important to emphasize that the SCI impact is an impact experiment on the surface of a real asteroid, i.e. at real asteroid scales and on a real asteroid material, allowing us to validate numerical simulations in the actual context of asteroid impacts and to compare with the prediction from the extrapolation of laboratory experiments and associated scaling laws. There are several previous explorations by means of a projectile impact on celestial solid bodies to study their surface materials, e.g. the NASA LCROSS mission on the moon tried to search for water in the regolith layer (Colaprete et al. 2010; Schultz et al. 2010), and the NASA Deep Impact mission on a comet observed a ejecta curtain and a vapor plume caused by a projectile impact and used the evolution of the ejecta curtain to establish the nature of the surface (porosity), gravity, and crater size (e.g., A'Hearn et al. 2005; Schultz et al. 2007; Richardson et al. 2007). The SCI impact is recognized as a

series of this type of active exploration on the surface of solid bodies, but it has an observational advantage for the cratering process compared to the previous explorations because *Hayabusa2* will closely observe the artificial crater during the sampling, and a Deployable CAMera-3 (DCAM3) will be released from the mother ship to observe the ejecta curtain with a high resolution during the crater formation. The SCI impact on Ryugu thus offers a great opportunity to study the impact crater formation process on a real asteroid in its low gravity environment.

In this paper, we introduce the scientific objectives, the expected results, and the observation plan of the SCI impact. Based on the concept described here, we will prepare for the SCI operations to maximize its scientific results.

2 Scientific Objectives of SCI Impact Experiment

From a point of view of impact experiments in space, the scientific objective for the SCI impact on Ryugu is to understand the impact process on a small asteroid. In other words, the SCI impact allows us to understand how impact processes are affected by the asteroid surface conditions and to construct the impact scaling laws directly applicable to real asteroids. In this section, we describe the target structure model for Ryugu and the scaling laws for impact cratering, the main scientific objectives of the SCI impact experiment being to evaluate the reliability of these scaling laws and to offer a validation point for numerical simulations of the asteroid impact process.

2.1 Surface Structure of Asteroids

One of the scientific objectives of the SCI impact is to obtain crucial information of the surface geology and the subsurface structure at and closed to the impact point on Ryugu. Recent explorations of asteroids by space-crafts such as *Hayabusa* (JAXA) and NEAR-Shoemaker (NASA) revealed that asteroid surfaces are generally covered with a regolith layer with boulders, even on asteroids as small as the 320 m-diameter (25143) Itokawa (Fujiwara et al. 2006; Miller et al. 2002; Veverka et al. 2001a). On Itokawa's surface, the close up images show that smooth terrains are filled with centimeter sized pebbles, while rough terrains contain meter to decameter sized boulders. The surface of (433) Eros observed in details for one year by the NASA NEAR-Shoemaker spacecraft showed a typical cratered geology on airless bodies, but its surface regolith layer composed of granular particles was found to be dynamically transferred toward the topographic low potential regions (Veverka et al. 2001b). This motion might be triggered by a high velocity impact of a small asteroid projectile on Eros. The high velocity impact may produce an impact induced seismic wave that could vibrate the regolith layer and fluidize the particles moving toward gravity-low (Richardson et al. 2005). In terms of low-gravity environment, the surface geology of Ryugu may be close that of Itokawa because both are in the few hundred meter-size range. However, Ryugu is a C-type asteroid, while Itokawa (and Eros) are S-type asteroids. The main belt asteroid (253) Mathilde is the only C-type asteroid for which we have a direct image obtained during a flyby by NEAR-Shoemaker, and its bulk density has been measured and found to be low with a value of 1.3 g/cm^3 (Yeomans et al. 1997; Helfrich et al. 1997). Such a low bulk density suggests that a large amount of porosity exists inside Mathilde. Asteroid porosity is usually classified into two categories theoretically: one is a micro-porosity with a scale of constituting minerals and another is a macro-porosity with a scale of the constituting boulders and blocks (Britt et al. 2002). The latter category is typically associated with a rubble-pile structure as proposed for Itokawa with a low density of 1.9 g/cm^3

(Fujiwara et al. 2006) compared to meteorite analogues. We are not sure whether Mathilde's low density comes from a rubble-pile structure and/or from micro-porosity, but it is probably reasonable to assume the presence of both micro- and macro-porosity in the internal structure of Mathilde. Since both Ryugu and Mathilde are C-type asteroids, then we consider the possibility of the presence of both micro- and macro-porosity for the interior structure of Ryugu. In fact, a rubble pile structure is even more likely for Ryugu given its small size. In effect, most bodies smaller than 50 km in size are at least of second generation given their short collisional lifetime (Bottke et al. 2005) and are therefore produced by the catastrophic disruption of a larger parent body. Numerical simulations of catastrophic disruption then indicate that most fragments larger than a few hundred meters are produced by gravitational reaccumulation of smaller pieces and consist of rubble piles (e.g. Michel et al. 2001; Jutzi et al. 2010), which should then apply to Ryugu. Regarding the micro-porosity in Ryugu, we need to note that the sizes of the constituting particles are quite important to control the porosity. It is well known that an assemblage of small particles like a powder with a size of sub μm is difficult to compress and the pores in the powder are difficult to squeeze out below the porosity of 60 % because of the strong friction and adhesion force between the constitutive particles with the size of sub μm caused by van der Waals force and hydrogen bonding (Yasui and Arakawa 2009). The friction and adhesion force are expected to effectively work on small asteroids in their low-gravity environment (Scheeres et al. 2010) and would easily sustain a highly porous structure above the porosity of 70 % (Kiuchi and Nakamura 2014). Since we have no information on the interior structure of Ryugu at present, we can only predict it according to various studies of asteroids and theoretical considerations on granular matters with the reference of the basic information and the assumption of the asteroid Ryugu: the asteroid shape is observed to be almost spherical; the speculated diameter is about 900 m; the rotation period is observed to be 7 h 38 min; the mass of the asteroid is estimated to be between 1.7×10^{11} and 1.4×10^{12} kg when the mean density is assumed to be between 0.5 and 4.0 g/cm^3 ; so the gravity acceleration and the escape velocity are between 6.1×10^{-5} and 4.9×10^{-4} m/s^2 and between 0.22 and 0.65 m/s , respectively, and the geometric albedo is 0.047 ± 0.003 (Ishiguro et al. 2014). Table 1 shows the predicted surface geology of Ryugu in the scale of the decameter area corresponding to mainly the excavated plus ejecta-deposited area of the SCI impact. In this table, the surface geology is firstly classified according to the size of regolith constituents composing the surface layer, then the constituent size is compared to the SCI impactor with a size of ~ 10 –20 cm.

2.2 Surface Models Expected for Ryugu

We defined a single block as a rock with a size larger than 1.5 m because the SCI projectile could not completely disrupt a block of this size; so it might rather form a simple crater on the block or partially disrupt the block (Fig. 1 and Table 1). In this category, the surface type is characterized by the cohesive strength and the porosity less than 40 %. Next, we define a granular layer as a layer with constituent sizes from 1 mm to 1.5 m. The minimum size of 1 mm in this category might be the particle size for which van der Waals force is almost comparable to the gravity force on Ryugu. We divide the granular layer category into three subcategories depending on the constituent size: a coarse-grained layer (particle size of 1 mm–5 cm), a pebble layer (particle size of 5–15 cm) and a boulder field (boulder size of 15 cm–1.5 m). These subcategories can be compared with the SCI projectile's size, which is larger than constituents of a coarse-grained layer, and almost comparable to pebble sizes (Fig. 1 and Table 1). In the case of the boulder field, a typical boulder size is larger than the SCI projectile's size, but enough small to be catastrophically disrupted by the impact. Finally, we define a fine-grained layer with a size of constituents smaller than 1 mm;

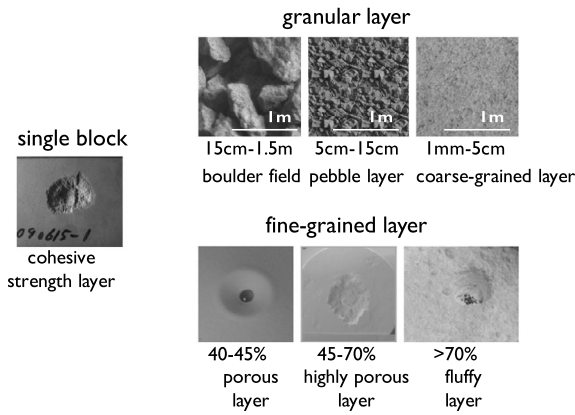


Fig. 1 Typical images of 7 subclass surfaces for Ryugu described in Table 1. Basalt block is shown as an example of the cohesive strength layer of single block, and it was impacted to form an impact crater. Basalt impact fragments are shown in the boulder field and the pebble field of the granular layer, and the scale bar is inserted in each photo. Coarse-sand is used in the coarse-grained layer with the scale bar. Glass beads are shown in the porous layer and sub-micron silica dust particles are shown in the highly porous and the fluffy layer. The highly porous layer looks strong because of the strong adhesion forces among sub-micron dust particles causing the high tensile strength of this layer

Table 1 Surface classification of Ryugu according to the size of constituents and the porosity

Class	Subclass	Crater size ^a	Scaling laws
Single block (> 1.5 m) ^d	Cohesive strength layer ($\phi < 40\%$)	70 cm–10 m	Strength
Granular layer (1 mm–1.5 m) ^d	Boulder field (15 cm–1.5 m) ^d	<15 cm–1 m	Strength
	Pebble layer (5–15 cm) ^d	2–10 m	Gravity
	Coarse-grained layer (1 mm–5 cm) ^d	2–>10 m	Gravity
Fine-grained layer (<1 m) ^d	Porous layer of $\phi = 40\text{--}45\%$ ^b	1–10 m	Gravity + strength
	Highly porous layer of $\phi = 45\text{--}70\%$ ^b	30 cm–1 m	Gravity + strength
	Fluffy layer of $\phi \geq 70\%$ ^b	<40 cm	Strength + gravity ^c

^aAn expected crater size is shown in the third column together with the scaling law applicable to each subclass in the last column

^b ϕ is the porosity

^cThe situation of wall collapse might occur

^dThe numbers in the parenthesis of the first and second columns are the size of the constituent materials. The definition of the size range for boulder and pebble is different from the conventional definition in sedimentology

so that fine-grained particles can be tightly stuck together by adhesion forces (Fig. 1 and Table 1). We subdivide this category as a function of the considered porosity: a porous layer has a 40–45 % porosity, a highly porous layer has a 45–70 % porosity, and a fluffy layer as a porosity >70 %. It is well known that aggregates made of equal sized spheres in a random close packing have a porosity of about 40 %. Therefore, we can suppose that a porous

layer with this fraction of porosity is an incompressible layer when the constituent materials behave as a rigid unbreakable matter. This incompressible layer is usually very well approximated by sand and glass beads in the laboratory. On the other hand, it is expected that the highly porous layer can be compacted by the crushing of its pores through the rearrangement of the particles when the applied stress is beyond the compressive strength of the layer supported by the adhesion forces among the particles. The layer can then be densified by compaction. Moreover, the fluffy layer can also be compacted, but the compressive strength of the fluffy layer is quite small compared to that of the highly porous layer, and therefore we expect the crater structure formed on this layer not to be sustained for a long time against the external perturbation.

These 7 types of surface structures cover reasonably well the range of possible surface structures of Ryugu. We thus study the crater formation process considering these 7 structures so that we can predict the various features of the resulting crater and ejecta curtain as a function of these structures before the SCI impact experiment is carried out on the asteroid.

2.3 Crater Scaling Laws

The impact cratering process on planetary bodies has been studied for several decades, and crater scaling laws were proposed to describe the crater size and the ejection velocities of excavated materials on various surfaces. Housen and Holsapple (2011) summarized their scaling laws based on a point source approximation with a key parameter called the coupling parameter, $C = a\delta^v U^\mu$, where a is the projectile radius, δ is the projectile density, U is the impact velocity, and μ and v are material constants determined by laboratory experiments. In addition to the coupling parameter, there are other physical parameters controlling the crater formation process such as the gravity g , the target density ρ , and the strength Y . The gravity mainly controls the cratering process for large scale impacts or even for small scale impacts on non-cohesive materials. On the other hand, the material strength mainly controls the cratering process for cohesive materials in small scale impacts. Therefore, the scaling laws are chosen according to the dominant mechanism for the cratering process. In the gravity regime, the scaling laws for the crater size and the ejecta velocity distribution are described as follows,

$$R \left(\frac{\rho}{m} \right)^{1/3} = H_1 \left(\frac{\rho}{\delta} \right)^{(2+\mu-6v)/[3(2+\mu)]} \left[\frac{ga}{U^2} \right]^{-\mu/(2+\mu)}, \quad (1)$$

$$\frac{v_e}{\sqrt{gR}} = C_2 \left(\frac{x}{R} \right)^{-1/\mu}, \quad (2)$$

where R is the crater radius, m is the projectile mass, U is the impact velocity, v_e is the ejection velocity of ejecta material excavated at a distance x from the impact point, C_2 is described as $C_2 = C_1 \left(\frac{4\pi}{3} \right)^{1/3} H_1^{-(2+\mu)/2\mu}$, and H_1 and C_1 are constants determined by laboratory experiments for each material. In the strength regime, the scaling laws are described as follows,

$$R \left(\frac{\rho}{m} \right)^{1/3} = H_2 \left(\frac{\rho}{\delta} \right)^{(1-3v)/3} \left[\frac{Y}{\rho U^2} \right]^{-\mu/2}, \quad (3)$$

$$v_e \sqrt{\frac{\rho}{Y}} = C_3 \left(\frac{x}{R} \right)^{-1/\mu}, \quad (4)$$

where C_3 is described as $C_3 = C_1 \left(\left(\frac{4\pi}{3} \right)^{\frac{1}{3}} H_2 \right)^{-1/\mu}$, and H_2 is a constant determined by laboratory experiments for each material.

Although laboratory impact experiments have been conducted for several decades, they have been limited to a small variety of targets (excepting the study by Schultz and Gault 1985); so that the parameters necessary for the scaling laws such as H_1 , H_2 , C_1 , μ and ν were only obtained for a limited set of targets and surface conditions. Therefore, it is important to determine these parameters for various targets and surface conditions that are expected on Ryugu in the laboratory. Then we can speculate about the subsurface properties of Ryugu by deriving the scaling law parameters such as H_1 , H_2 , C_1 , μ and ν from the DCAM3 observations of the ejecta curtain and the remote sensing observations of the crater morphology. Actually, if the SCI artificial crater is formed in the gravity regime, we will be able to determine C_2 and μ in Eq. (2) by means of the observation from the DCAM3, and then H_1 will be determined by the final crater radius observed by the remote sensing instruments according to Eq. (1), assuming ν is equal to 0.4 as is classically assumed (Housen and Holsapple 2011). The effect of the micro-gravity on the crater formation process is the most interesting issue in this experiment; so the scaling laws derived for Ryugu should be carefully compared with the laboratory experimental results. This will allow us to determine whether the SCI results can be explained by the difference of the constituent materials only or by a new discovery of the micro-gravity effects on the impact process. If the crater is formed in the strength regime, we will obtain the combined parameter of H_2 and Y according to Eqs. (3) and (4).

There were two famous space explorations involving an artificial impact crater in the past: they were the LCROSS mission on the moon and the Deep Impact mission on the nucleus of the comet 9P/Tempel-1. LCROSS observed the ejecta plume and found evidence of the artificial crater with a size of 20 to 30 m (Schultz et al. 2010). The large ejecta curtain was successfully observed by the Deep Impact mission, and later the Stardust NExT mission fortunately succeeded to find evidence of the artificial crater formed by Deep Impact on the nucleus of the comet, with a diameter estimated from 50 m to 200 m (Schultz et al. 2012). The contribution by Schultz et al. could identify a low-rimmed shallow crater surrounding a central strength-controlled pit. They concluded that the upper surface of loosely consolidated material acted as a gravity-controlled target (consistent with the amount of observed ejecta), whereas the smaller central pit was a strength-controlled crater. Moreover, Richardson and Melosh (2013) suggested the effective strength of the surface of comet 9P/Tempel 1 (1–10 kPa). Our impact experiment on Ryugu will be also observed with enough resolution to construct the scaling laws and to determine whether it is gravity or strength dominated.

Once we succeed in constructing the scaling laws regarding the crater size and the ejecta, we can apply these laws to various other problems involving celestial body impacts. The same applies to numerical simulations of the impact process, which, once validated by confrontation to this asteroid scale experiments, can be applied with greater confidence to other asteroid impact issues. For example, we can determine the age of asteroid surfaces with greater confidence. To do so, the best approach is to use the information provided by the crater distribution on the surface of the object, as will be imaged by *Hayabusa2* on Ryugu. Then, using an impactor flux model, the time needed to accumulate the craters on the asteroid surface can be calculated, taking into account several processes which can affect crater formation and crater erasure on such a low-gravity object, such as seismic shaking. However, a crucial element of this calculation is to derive the crater's size from the impactor's size. So far, classical scaling laws have been used to derive asteroid's ages, like Iotkawa (e.g. Michel et al. 2009), and thanks to the SCI experiment and the resulting improvement of our understanding of the impact process at asteroid scale, the refinement of scaling laws, and

the validation of numerical models, we will be able to use more reliable relations between impactor's size and crater's size, and therefore more accurate estimates of surface ages. Furthermore, we will be able to estimate the erosion and gardening effects on Ryugu using the newly constructed scaling laws combined with the analysis of returned samples.

3 Instruments

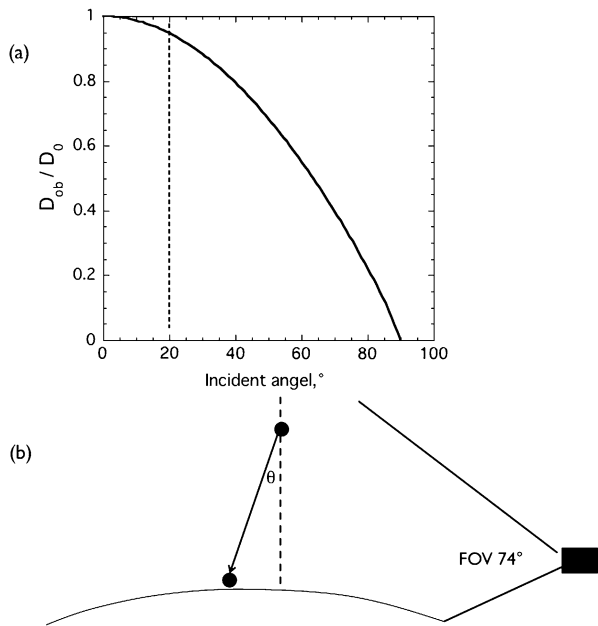
3.1 Small Carry-on Impactor

The Small Carry-on Impactor involves the launch of a copper projectile with a mass of 2 kg at an impact velocity of 2 km/s. The projectile has a shape of a spherical shell like a hollow ball with a thickness of about 5 mm and a diameter of 13 cm; so the effective density of this hollow ball is 2.3 g/cm³. The projectile is expected to impact the asteroid surface in the direction normal to the surface. However, the actual impact angle will be determined by the in-situ observations because the nutation of the SCI activated at the separation might cause an oblique impact on the surface although the local topography of the asteroid can cause an oblique impact. The detailed sequence of the SCI operations and other engineering aspects are reported in Saiki et al. (2016, in this issue). A performance test of the SCI in the real scale was conducted in a field to confirm the collimation and the cratering efficiency (Wada et al. 2014; Saiki et al. 2016, in this issue). This test showed us that the projectile flew straight in the errors within 1 degree and the impact crater was formed on a wet sand with a size of about 2 m under the earth's gravity. This crater size of 2 m formed on the sand is consistent with the crater size estimated from the conventional scaling law with the projectile density of copper material density, 8.9 g/cm³ and mass, 2 kg, and the effective density of this hollow ball is not suitable to explain the experimental result (Wada et al. 2014). However, the previous study suggested that the effective density of hollow projectiles was suitable for the conventional scaling law of the crater size (Schultz and Gault 1985), and then the more careful analysis should be necessary to confirm the result obtained by Wada et al. (2014) in the future.

3.2 Deployable CAMera 3-D

The Deployable Camera 3 (DCAM3) is a small camera with a size of $\sim\phi 78 \times 81$ mm that will be separated from *Hayabusa2* and observe the SCI impact event. DCAM3 has two camera systems: DCAM3-A and DCAM3-D. The former is a low-resolution, monitoring camera and the latter is a high-resolution camera specified for scientific observations of the SCI impact. We will use images taken by DCAM3-D to analyze the impact process of SCI. Since the details of the performances and operations of DCAM3-D are described by Ogawa et al. (2016, in this issue), a brief summary is described here. DCAM3-D is a wide-angle digital camera with a high-speed digital transmitter up to 4 Mbps developed to observe the SCI before explosion and the ejecta curtain. DCAM3-D is the only instrument that will conduct the in-situ, detailed observations of the SCI impact because *Hayabusa2* will escape behind the asteroid immediately after the separation of the SCI in order to avoid the possible collisions of debris generated by the SCI explosion. *Hayabusa2* will release DCAM3 in a mid-way of its escape, approximately at an extension of the horizon of Ryugu, 1 km away from the predicted point of the SCI impact. From that position, the resolution of DCAM3-D images is less than 1 m/pixel, which is enough to observe the ejecta curtain produced by the SCI impact as described in the next section.

Fig. 2 Effect of oblique impacts on crater size and a schematic illustration showing the definition of the incident angle. (a) The crater size obtained for the oblique impact is normalized by the crater size obtained for the normal impact according to Gault and Wedekind (1978). (b) The incident angle is defined as the angle between the impact direction and the normal direction to the surface. DCAM3-D is able to observe both the position of the SCI explosion launching the projectile and the impact point on the asteroid surface simultaneously because it has a wide FOV of 74°



3.3 Effect of Impact Angle on the Crater Formation

Because of the position and velocity errors of SCI at separation from the mother ship and the nutation of SCI itself, the actual impact point can scatter within a radius of 200 m from the target point where it sets the sight on (Saiki et al. 2016, in this issue). This means that the SCI projectile might obliquely impact on the asteroid surface. Moreover, it is very difficult to predict the surface local inclination relative to the impact direction. So, we must take into account the effect of impact obliquity on the crater formation process. Previous studies on oblique impacts have showed that the crater diameter gradually decreases with increasing incident angle of the projectile measured from the vertical line (Fig. 2a), and an incident angle larger than 20° has a great influence on the crater diameter (Gault and Wedekind 1978). Therefore, it is necessary to determine the incident angle of the SCI projectile to interpret correctly the impact outcome. To determine the incident angle, we must know both the point of launch and that of impact, that is, the position of the SCI explosion launching the projectile and the position of the artificial crater. DCAM3-D is required to have a wide field of view (FOV) of 74° for imaging both SCI before explosion and the impact point (Fig. 2b, and see also Ogawa et al. 2016, and Ishibashi et al. 2016, in this issue). The scale of SCI before explosion is about $\phi 30 \times 15$ cm, small compared to the pixel size of DCAM3-D imager at a distance of about 1 km. To clearly detect SCI in images of DCAM3-D, SCI is wrapped with Beta-cloth which has a diffusive reflectance of 80 % at visible wavelength. According to the optical configuration of DCAM3-D, we expect that SCI is detectable with $S/N > 5$ (see Appendix B for more detail). Although SCI before explosion is detected by DCAM3-D, the images can only determine the altitude of the SCI position. The horizontal position is estimated with images taken by onboard cameras, e.g., ONC, at the separation of SCI from the mother ship (Saiki et al. 2016, in this issue).

3.4 Observation with DCAM3-D and Other Onboard Sensors

As mentioned in the previous sections, the imaging objects of DCAM3-D are the SCI floating above Ryugu at an altitude of ~ 500 m before explosion, and the ejecta produced by SCI impact. SCI before explosion is bright owing to the wrapped Beta-cloth, but its imaging signal is small because it is smaller than the imaging resolution of DCAM3-D (~ 1 m/pixel). Ejecta is, on the other hand, expected to be dark, similar to or brighter than the surface of Ryugu, as mentioned below. The specification of DCAM3-D must be ready for those two objects of different brightness. In addition, to determine the impact point of SCI and the position of DCAM3-D itself from images, the surface of Ryugu should be also clearly imaged by DCAM3-D. The surface of Ryugu is dark with a geometric albedo less than 0.05 (Ishiguro et al. 2014), occupying about half the FOV of DCAM3-D. The radiance and the signal of the asteroid surface are estimated, assuming Hapke model (Hapke 2012) with Hapke parameters for Ryugu (Ishiguro et al. 2014), other C-type asteroids, and comets (Li et al. 2009). The predicted signals depend on the Sun distance and the phase angle of the Sun. In the case of a Sun distance equal to 1.25 AU and the phase angle to 20° , the surface of Ryugu is calculated to be imaged by DCAM3-D with signals in the range of 300–1500 electron/pixel, comparable or darker than the ejecta curtain (the signals for the ejecta curtain is expected to be 300–6000 electron/pixel as mentioned in Sect. 4.2). Consequently, we have prepared three imaging modes specialized for each imaging object: SCI mode, ejecta mode, and asteroid (Ryugu) mode. The setting of imaging parameters for each mode and the mixing sequence of these modes in the actual operation are described in Ogawa et al. (2016, in this issue).

The main instruments for remote sensing onboard *Hayabusa2* are a visible-band imaging camera ONC, a thermal infrared camera TIR, a near infrared spectrometer NIRS3, and a light detection and ranging LIDAR. These instruments will reveal the difference (or similarity) between the inner and outer regions of the crater formed by the SCI impact. In particular, ONC observations will bring us key data for the scientific topics described above, such as the morphology and the size of the newly formed crater, the distribution of ejecta deposits around the crater, the fragment distribution of disrupted boulders, and the detection of the surface motion caused by the impact. For those observations, it is important to take images both before and after the SCI impact with the same resolution, which should be as high as possible so that we can recognize the difference caused by the impact.

4 Theoretical and Experimental Studies on Prediction of SCI Impact and the Scientific Topics

4.1 Expected Crater Size

The crater size is one of the most important parameters to be measured in impact experiments. The crater formed by the SCI impact will be observed with the onboard cameras, i.e., ONC-T with the resolution of 10 cm/pixel at 1 km from the asteroid surface and the FOV of $6.35 \times 6.35^\circ$, and TIR with the resolution of 1 m/pixel at 1 km from the asteroid surface and the FOV of $16 \times 12^\circ$, when *Hayabusa2* comes back from its temporal escape several weeks after the SCI impact. We estimate the crater size formed by the SCI impact using the crater size scaling law described by Eq. (1) in the gravity regime, assuming that the asteroid surface is covered with a coarse-grained layer, a pebble layer or a porous layer (Table 1), and the effect of the oblique impact is also considered in Fig. 2a. Several parameters are

necessary for calculating Eq. (1), and they were obtained for a few non-cohesive materials such as sand in the previous studies, as summarized in Housen and Holsapple (2011). Here, we use conventional crater scaling laws for the following discussions to estimate the crater size and the ejecta velocity distribution though these laws might be refined depending on what is discovered during the SCI experiment.

The crater radius estimated for sand is about 5 m in the micro-gravity condition of Ryugu, and this estimate might be the maximum crater radius expected from the laboratory result. Recent impact experiments on sand showed that the crater size did not change so much even in the micro-gravity condition ($<10^{-5}$ G), that is, the crater size is about the same as that formed on the Earth (Takagi et al. 2007). In this case, the crater radius formed by the SCI impact might be about 1 m. However, we are not sure why this discrepancy occurred between the scaling law and the micro-gravity experiment. This issue could be clarified by the result of the SCI impact if the asteroid surface is covered with a coarse-grained regolith layer.

In the case of a boulder field, we expect that the impact energy of the SCI projectile is almost comparable to the disruption of each boulder, and therefore impact fragments would be ejected instead of the creation of a typical ejecta curtain. This means that an apparent impact crater is not formed in this boulder field, and instead, we would observe the disrupted fragments spread over the impact area. This subject is revisited later in Sect. 4.5.

When the SCI projectile impacts on a single block with a finite strength such as a cohesive material, the crater size is estimated by using Eq. (3) in the strength regime. In this case, the crater size strongly depends on the material strength, and the crater radius is estimated to be about 0.7 m for the high strength layer of typical terrestrial rocks, like basalt. As the crater size becomes larger with decreasing material strength, we expect in this case the surface strength to be determined from the crater radius produced by the SCI impact.

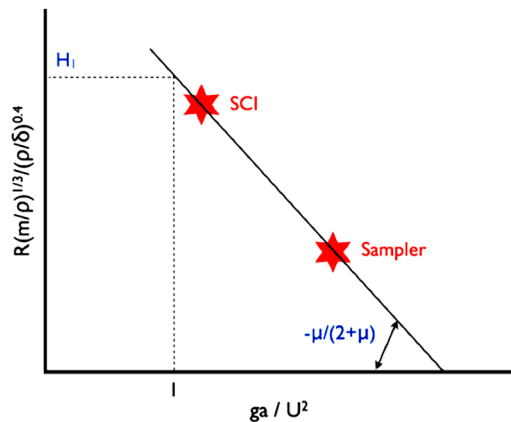
In the case of a highly porous layer with a porosity of 45–70 %, a crater formed by compaction can be formed, with pore crushed, inside. Schultz and Gault (1985) made cratering experiments on a compacted pumice with the density of 1.28 g/cm^3 and found the low cratering efficiency to a sand target with the density of 1.55 g/cm^3 , and the low density of the pumice target compared to the sand target might mean that the pumice grains had a large porosity inside; so the low cratering efficiency on the compacted pumice target might be caused by the energy loss during the crush of pumice grains. On the other hand, according to impact experiments on porous gypsum block with a porosity of 50 %, the crater diameter defined by the spallation diameter is found to be several times as large as the projectile diameter (Fig. 3). In this case, the crater radius might be smaller than 1 m. Spallation is usually observed on surfaces made of cohesive materials with relatively high strength of a few MPa such as porous gypsum block, but we are not sure that spallation will occur on Ryugu. However, the pit is a deep hole that can be recognized easily on a highly porous layer, and the pit diameter is found to be a few times as large as the projectile diameter (Yasui et al. 2012). Thus the pit diameter formed by the SCI impact might be less than from 30 to 40 cm. This is the minimum estimate for the artificial crater formed by the SCI impact.

In the case of a fluffy layer with a porosity larger than 70 %, we speculate that the compressive crater without a spallation region and a distinguishable ejecta deposit could be formed because of the weak strength of the layer, and the deep pit would be only observed at the impact area as was observed by Housen et al. (1999). The estimated pit size formed by the SCI impact could be similar to that of the pit formed on the highly porous layer, thus the size might be smaller than 40 cm. Furthermore, since the wall of the deep pit on a fluffy layer would easily collapse by perturbation, the pit might eventually be buried by the debris of the collapsed wall. Therefore, the SCI impact crater might be difficult to recognize on a

Fig. 3 Picture of the impact crater formed on a porous gypsum target with a porosity of 50 %. An aluminum spherical projectile with a diameter of 3.2 mm made an impact at a velocity of 2 km/s and a vacuum condition below 10 Pa. A deep pit with a diameter of 9 mm and a shallow spall region around it are observed



Fig. 4 Relationship between π -scaling parameters for the gravity regime. Two artificial craters with very different sizes are expected to be formed by the SCI and the sampler projectile. They can both be used to construct the scaling law for crater size of Eq. (1) in the gravity regime

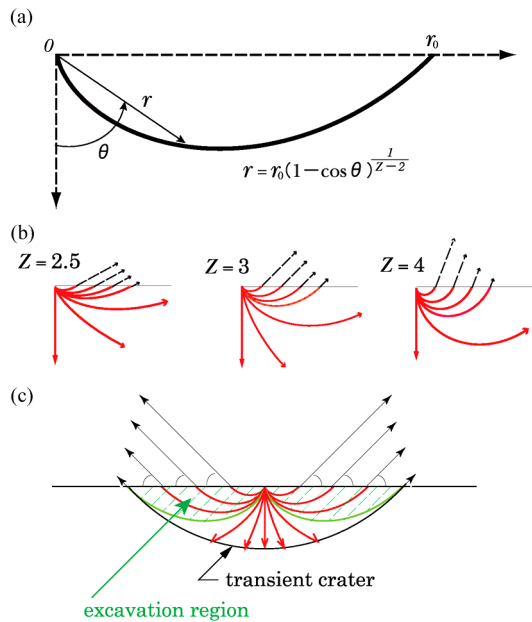


fluffy layer. However, Schultz et al. (2005) showed that oblique impacts into highly porous target composed of perlite grains with a bulk density of 0.2 g/cm³ resulted in significant excavation and in a larger crater compared to that formed by normal impacts. Moreover, Schultz et al. (2012) showed that the crater was clearly recognized on a fluffy surface when the target surface had a layered structure. Therefore, the SCI impact crater might be recognized when the projectile is obliquely collided on a fluffy layer and/or on a surface with a layered structure.

The most interesting expected result from the SCI impact is the effect of the microgravity on the cratering process as is written by Eq. (1). We have another opportunity to study the microgravity effect directly in the framework of the *Hayabusa2* mission. The sampler on *Hayabusa2* plans to launch a projectile made of tantalum of 5 g with a size of $\sim\phi 8 \times 10$ mm, then a small crater will be formed that will eject surface materials and some of this material will be collected through the sampler horn. This sampler provides us another opportunity to form an impact crater at a much smaller impact energy than the SCI impact. In addition to the SCI impact crater, we can use this small crater formed by the sampler projectile in the elaboration of the scaling laws for the crater size when the physical properties of the sampling site and the SCI impact site are similar. The crater scaling law of Eq. (1) can be refined further as shown in Fig. 4.

Fig. 5 Maxwell’s Z model.

(a) A stream line, represented by the equation in the polar coordinate (r, θ) , crossing the original target surface at a distance r_0 . (b) Stream lines for the cases $z = 2.5, 3,$ and 4 . In the case of $z = 3$, the ejection angle is 45° and the ejection velocity decreases with r^{-3} . (c) Excavation region, in which materials within a transient crater are ejected beyond the original target surface



4.2 Growth of Ejecta Curtain: Angle of Ejecta Curtain, Ejection Angle and Velocity Distribution of Ejecta Particles

One of the most important objectives of the SCI impact experiment is to observe an ejecta curtain and dust excavated from the artificial crater. This observation will be realized with DCAM-3D. There is a simple model called the Z-model showing the flow field below the impact area activated by a high velocity impact (Maxwell 1977; Croft 1980). The Z-model assumes an incompressible flow with a point source located at the impact point on the surface such as a coarse-grained layer and a fine-grained porous layer. In the incompressible flow, the radial particle velocity u_r is assumed to decay with the radial distance r according to the following equation

$$u_r = \frac{\alpha}{r^z}, \tag{5}$$

where α is the intensity of the flow field and z is the power law index of the decay. Based on this model, the flow line can be calculated for various values of z (Fig. 5), and the ejection velocity and angle of excavated materials are estimated. Comparing the formulation of the Z model to the π scaling law described by Eq. (2) or (4), we can notice that μ in the coupling parameter of the π scaling law corresponds to $1/z$ in the Z model, and the ejection angle θ of ejecta particles is related to μ as $\tan \theta = 1/\mu - 2$. When the value of z is chosen to be 3, θ is equal to 45° . Since the observed ejection angle in laboratory experiments is approximately 45° for sand targets, a typical value of z is considered to be 3. Then, the ejecta curtain is simulated by using the typical ejection angle of 45° together with other parameters necessary for the ejecta scaling law of Eq. (2) in the gravity regime in Fig. 6. We assume a typical sand target with parameters of $C_2 = 0.64$ and $\mu = 0.41$ (Housen and Holsapple 2011). Figure 6 shows the cross section of the ejecta curtain changing with time normalized by the crater growth time T for a typical sand target and a surface gravity of $2.6 \times 10^{-4} \text{ m/s}^2$, where the final crater radius is assumed to be 5 m and the ballistic trajectory is assumed for each grain

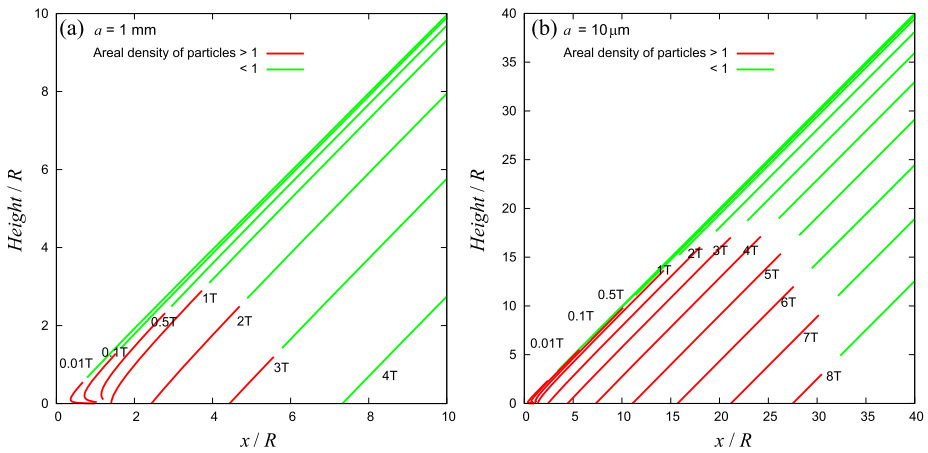


Fig. 6 The cross section of the ejecta curtain proceeding with time, assuming a typical sand target ($C_2 = 0.64$ and $\mu = 0.41$), and the radius of constituent ejecta particles is (a) 1 mm and (b) 10 μm . The horizontal axis shows the distance x from the impact point and the vertical axis shows the height from the target surface, both being normalized by the final crater radius R . The time labeled for each curtain is normalized by the crater growth time $T = 0.92(R/g)^{1/2}$ for a typical sand target, where g is the surface gravity (Holsapple and Housen 2007). With g and R being $2.6 \times 10^{-4} \text{ m/s}^2$ and 5 m, respectively, T is calculated to be 128 sec. The red lines show a dense part of curtains with an areal density of particles > 1 , while the green lines show a sparse part

(T is calculated to be 128 sec with a scaling law shown in Holsapple and Housen 2007). Both axes are normalized by the final crater radius and the origin is defined to be the impact point. After $1T$, the ejecta curtain is found to fall down toward the asteroid surface, then the ejecta curtain gradually departs from the crater beyond $7R$ at $4T$. The visibility of the ejecta curtain from DCAM3-D is inspected in Fig. 6 according to the areal density of the ejecta particles with a size of 10 μm and 1 mm. We suppose that the ejecta curtain could be easily observed at the region where the areal density is larger than 1, that is, most of the incident sun light would be scattered on the curtain surface. According to this simple estimation, the visible area of ejecta curtain is more than about 100 m for 10 μm particles compared to that for the 1 mm particles of about 20 m. Recently, a more realistic prediction of the visibility of the ejecta curtain has been proposed based on numerical calculations of the scattering of the incident sun light (Shalima et al. 2015), resulting in about 0.3–60 $\text{W/m}^2/\text{sr}/\text{micron}$ at a wavelength of 550 nm at the Sun distance of 1 AU. Using this estimate, we calculate the imaging signal with the actual optical properties of DCAM3-D (Ishibashi et al. 2016, this issue) as about 300–6000 electron/pixel at the Sun distance of 1.25 AU. Since the full well of DCAM3-D imager is 21,000 electron/pixel and its linearity range is $< 11,000$ electron (Ishibashi et al. 2016, this issue), DCAM3-D is able to detect the ejecta curtain with sufficient S/N ratio.

One of the scientific purposes of the ejecta curtain observation by DCAM3-D is to determine the scaling law for the ejecta velocity distribution on Ryugu. In order to construct the scaling law, we need to know the relationship between the ejection velocity of each particle and the ejection distance from the impact point (e.g. Hermalyn and Schultz 2011). However, it is not easy to deduce the relationships from the successive images of the ejecta curtain. We are studying how to deduce the velocity distribution of ejection particles from the ejecta curtain images. The elementary processes related to the ejecta curtain formation have been studied by Tsujido et al. (2015), then the ejecta curtain angle is found to be de-

Fig. 7 Schematic illustration showing the relationship between (a) the ejecta curtain angle β and the ejecta velocity distribution v_0 , and between (b) the ejecta curtain angle and the ejection angle of regolith particles θ

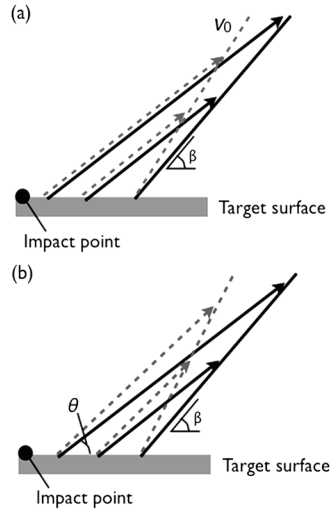
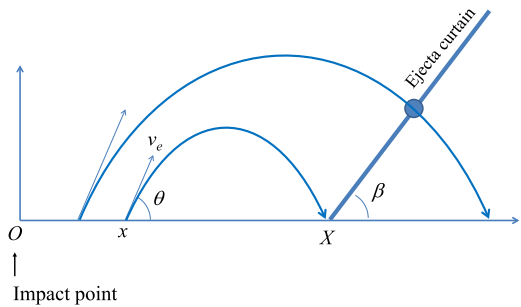


Fig. 8 Cartoon showing parameters related to the ejecta curtain. Particles on the target surface are ejected at a distance x from the impact point at the ejection velocity v_e and angle θ , respectively. When they land at a distance X , the position of the ejecta curtain is given as delineated with the angle β



terminated by the ejection angle of each particle and the decay rate of the ejecta velocity distributions (Fig. 7) although the angle of the curtain is also controlled by topography and early-time compressibility, and strength. Moreover, the simple ballistic trajectories of ejecta grains with an ejection velocity v_e and angle θ , depending on the initial position x are analyzed theoretically with a new simple theory predicting the ejecta curtain geometry. That is, the local curtain angle β where the curtain contacts on the surface and the horizontal velocity \dot{X} of the contact position of the ejecta curtain provide the ejection angle of particles at each initial position (Fig. 8, see Appendix A for derivation)

$$\frac{1}{\tan \theta} + \frac{1}{\tan \beta} = \frac{2\dot{X}}{gt}, \tag{6}$$

where t is the laps time after the impact and g is the gravity acceleration on the asteroid surface. Once the ejection angle θ at each original position is estimated, we could estimate the ejection velocity at each position using the simple equations of ballistic motion, then we obtain an ejecta velocity distribution. This simple method proposed by Wada is called ‘‘Wada’s method’’ and it will be improved in the future for the practical use of the ejecta curtain analysis from DCAM-3D (Tsujido et al. 2013). If the scaling law is obtained for the gravity regime on Ryugu, it will be a very good opportunity to elucidate the effect of the microgravity on the ejecta velocity distribution, and then μ and C_2 in Eq. (2) could be determined for the first time in a microgravity condition.

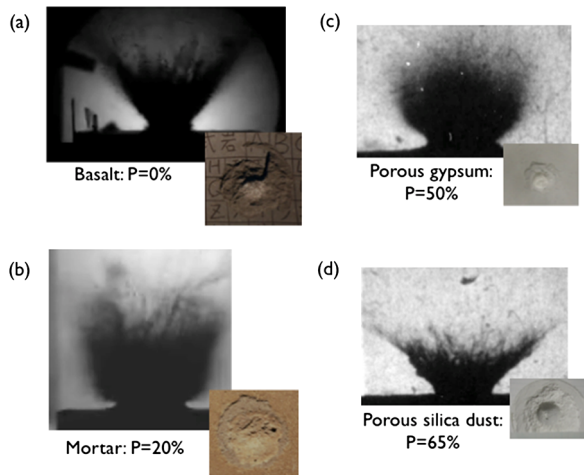
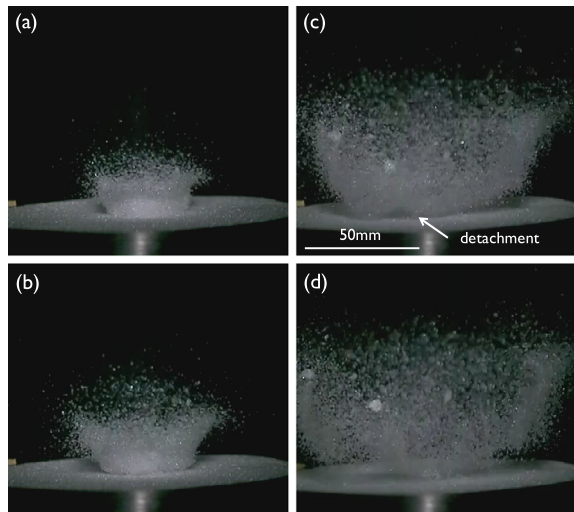


Fig. 9 Ejecta curtain shapes depending on target materials. **(a)** Basalt, **(b)** Mortar with a porosity of 20 %. These curtains were formed on a single block impacted at 4 km/s by a nylon spherical projectile with a size of 7 mm. **(c)** Porous gypsum with a porosity of 50 %, **(d)** Porous silica dust with a porosity of 65 %. These curtains were formed on a fine-grained layer impacted at 3.2 km/s by a nylon projectile. The insets are the photos of final craters formed by each impact

When the asteroid surface has a mechanical strength which is large enough to compare well with the subsurface stress exerted by the self-gravity, the crater formation process including the ejection of the disrupted fragments and the final crater size are mainly controlled by the material strength according to Eqs. (3) and (4). In the strength regime, the morphology of the ejecta curtain is full of variety depending on strength and other properties such as the porosity and the constituent size (Fig. 9). Figure 9 shows a snap shot of the ejecta curtain formed on various surfaces with different porosities and mechanical strengths. The ejecta curtains formed on a single block are shown in Fig. 9(a) and (b), and we can recognize a typical conical shape curtain for the basalt target without porosity, but for the mortar target with a porosity of 20 %, the shape of the ejecta curtain looks like a hanging bell and the outline of the curtain is very diffuse. Moreover, the curtain shape of the fine-grained layer is also found to depend on the porosity. Figure 9(c) and (d) show the ejecta curtains observed for the highly porous layers with a porosity of 50 % and 65 %. The curtain shape of the porous gypsum is similar to that of the mortar, and that of the porous silica dust is similar to the basalt although the curtain angle is different. There is little studies on the ejecta curtain of cohesive materials with various strengths; so, we will intensively study the ejection process of impact fragments from cohesive materials with the variety shown in Fig. 1 and clarify the ejection mechanisms causing the variety of the curtain shapes. Then, we elaborate the scaling law for the ejecta velocity distribution to compare it with the ejecta curtain on Ryugu and this comparison will give us the crucial information on the subsurface structure of the asteroid.

The most apparent difference of the ejecta curtain in the strength regime from that in the gravity regime is a detachment of the ejecta curtain from the surface as shown in Fig. 10. This picture clearly shows the boundary between the target surface and the base of the ejecta curtain, and the base of the curtain moves upward with some velocity depending on the mechanical strength while the ejecta curtain never detaches from the surface for the non-cohesive material in the gravity regime. But, it should be noted that strength still could

Fig. 10 Typical ejecta curtain showing detachment from the target surface at the base of the curtain. A sintered snow target with a porosity of 36 % was impacted to form the detached ejecta curtain. The time after the impact in each photo is (a) 10 ms, (b) 17 ms, (c) 30 ms, (d) 45 ms



affect crater growth without causing detachment of the ejecta curtain. This happens as inter-particle friction slows growth but doesn't result in detachment. Figure 11 shows the time sequence of the ejecta curtain simply calculated with the different mechanical strengths. In this calculation, the ratio of the typical ejection velocity in the strength regime to that in the gravity regime described by $\sqrt{Y/\rho g R}$ is changed from 1 to 10^3 together with the change of the crater formation time T from 27.3 s to 0.0273 s depending on the crater size. It is noticeable that the base of the ejecta curtain detaches from the surface with a velocity comparable to $\sqrt{Y/\rho}$. So, when $\sqrt{Y/\rho g R}$ is larger than 10^3 corresponding to the mechanical strength of a few MPa, the base of the ejecta curtain leaves away from the surface farther than 1000 m within several seconds. The FOV and the framing speed of DCAM3-D are designed to observe not only a typical ejecta curtain in the gravity regime but also a high velocity ejecta curtain (1 frame per second; Ogawa et al. 2016, in this issue). The areal density larger than 1 is also shown in Fig. 11, and we can recognize that it is difficult to observe the ejecta curtain in the strength regime because of the high ejection speed and the short observation time within the FOV.

4.3 Ejecta Deposits Around the Crater

The low velocity materials ejected from the crater formed by SCI would deposit around the crater, making a crater rim and an ejecta deposition layer. The rim and ejecta deposition region is one of the candidates for sampling after the SCI impact experiment. We suppose that the material coming from larger depth is more fresh compared to the outermost material because it could be relatively protected from space weathering, and our project expects to recover the material originating from the greatest possible depth. We are, therefore, very interested in assessing the original depth of the recovered sample and thus we calculate the ratio of the constituting materials excavated from different depth in an assemblage of the recovered sample as follows.

First, according to the Z model together with the scaling law for the velocity distribution, we calculate the thickness of the deposits changing with the distance from the crater edge for the crater formed in the gravity regime. We also estimate the maximum depth of the excavated materials deposited at each distance, provided that ejected materials do not

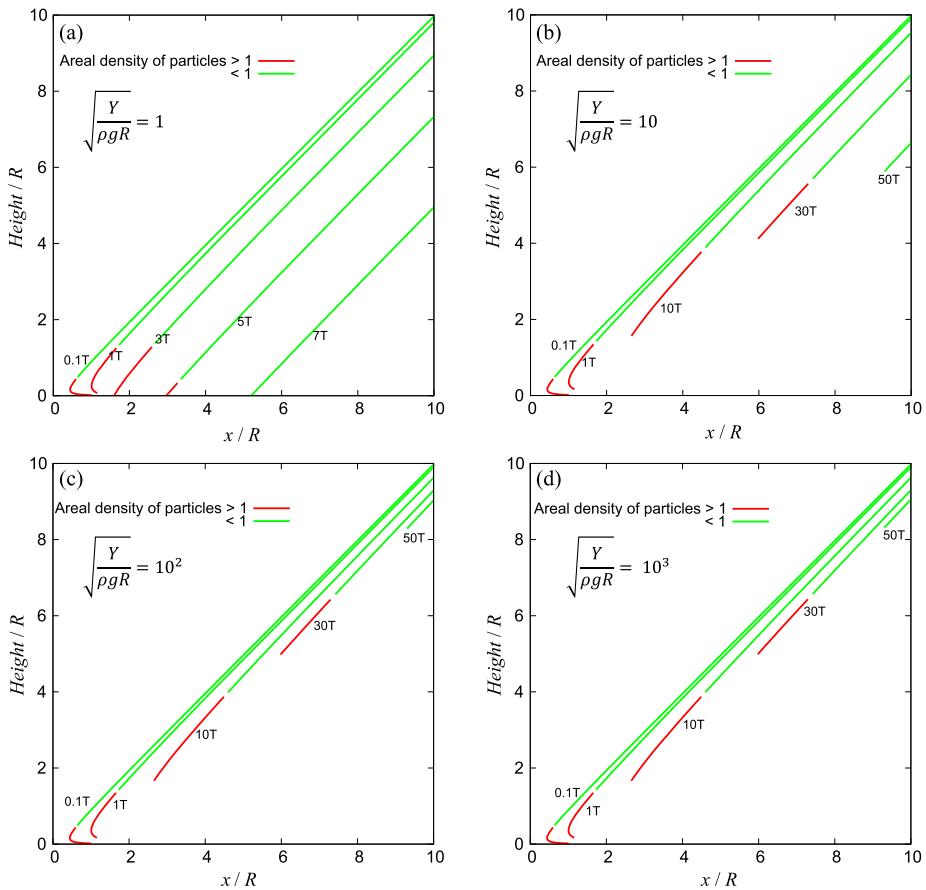


Fig. 11 Same as Fig. 6, but assuming the strength regime scaling law with parameters of $C_3 = 0.53$ and $\mu = 0.55$ (Housen and Holsapple 2011). The ejecta curtains proceed differently, depending on the target strength Y with $(Y/\rho g R)^{1/2} =$ (a) 1, (b) 10, (c) 100, and (d) 1000. The crater growth time T is given by $T = 0.44R/(Y/\rho)^{1/2}$ for a typical rock target (Holsapple and Housen 2007). Here we assume $R = 1$ m, then (a) $T = 27.3$ sec, (b) 2.73 sec, (c) 0.273 sec, and (d) 0.0273 sec. When giving the areal density of curtains, we assume the radius of the constituent ejecta particles to be 1 mm

horizontally move after landing on the surface. For instance, Fig. 12 shows the thickness of the ejecta deposit, h , which corresponds to the rim thickness, and the maximum depth of the excavated material deposited, H_{exc} , changing with the distance from the impact point, x , where the typical sand values for the constants required for the scaling law and the Z model were used: μ is 0.41, C_2 is 0.64, and R is 5 m. Then, h drastically drops within $2x/R$, and the thickness is estimated to be about 10 cm at 9 m ($1.8x/R$) from the impact point. On the contrary, H_{exc} does not significantly depend on the deposited distance beyond $1.5x/R$, then H_{exc} is estimated to be about 1 m depth at 9 m from the impact point.

Second, we estimate the ratio of the constituting materials excavated from different depth, provided that the ejecta layer is so mixed that the order of stratification at deposition cannot be preserved at all. Figure 13 shows the estimated ratios of the sample recovered from the surface layer above 5 cm at different distance from 7.5 m to 15 m from the impact point. It is recognized that the sample is recovered from not only the rim deposit but also the pre-impact

Fig. 12 Thickness of the ejecta deposit, h , and maximum depth of the excavated material deposited, H_{exc} , as a function of the distance from the impact point, x . These parameters are normalized by the crater radius R . Here we assume the scaling law for a typical sand ($\mu = 0.41$, $C_2 = 0.64$, and $R = 5$ m) and the Z model with $z = 3$

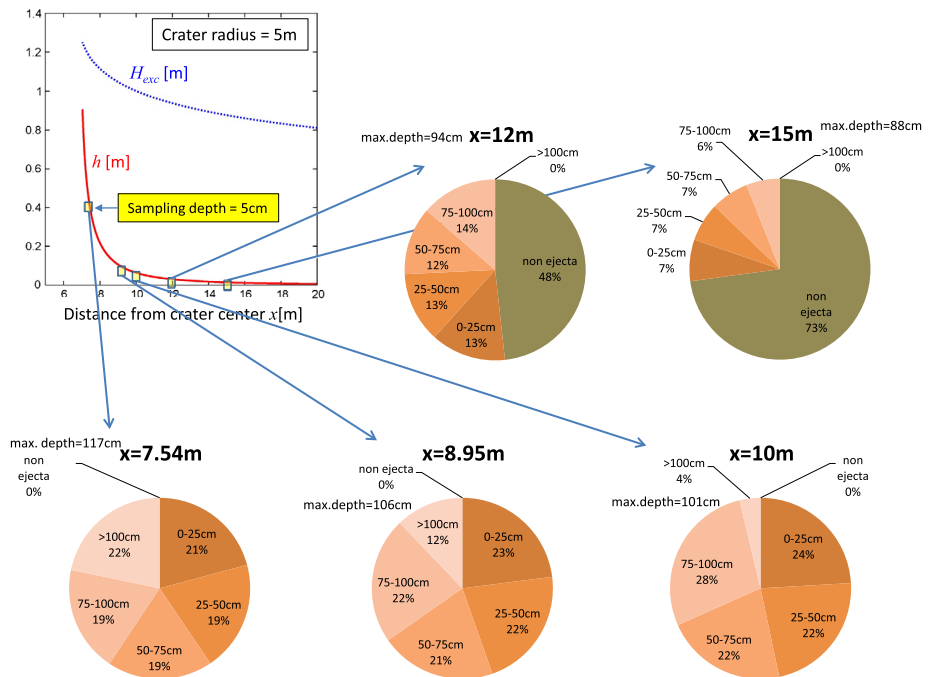
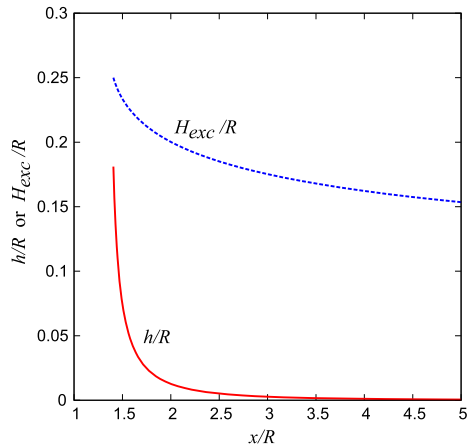
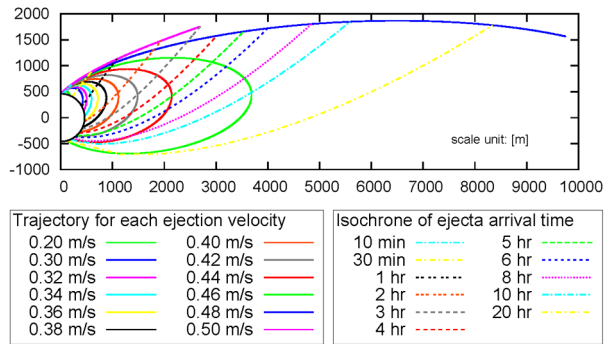


Fig. 13 Estimated fractions of the original depth of the sample materials recovered from the surface layer down to 5 cm at different distances from 7.5 m to 15 m from the impact point. Non-ejecta means the sample from the pre-impact surface below the rim deposit

surface below the rim deposit when the rim thickness is thinner than 5 cm. The fraction of the deepest materials, which here we define as materials excavated from depth of > 100 cm, changes from 22 % to 4 % with an increase in the distance from 7.5 m to 10 m, and we never recover the deepest materials at the distance farther than 12 m. Since these results are sensitive to the constants required for the scaling law and the Z model, these constants should be obtained by the observation and the analysis that are described before.

Fig. 14 Trajectory for each ejection velocity of ejecta (*solid lines*) and isochrones of ejecta arrival time (*dashed lines*) in the case of an impact into a sand surface of Ryugu (A *half circle* denotes Ryugu and the impact point is at (0, 500)). Here, for simplicity, we assume the ejection angle is 45° and we ignore the spin of the asteroid and the effect of the solar radiation pressure



Michel and Delbo (2010) investigated the orbital and thermal evolutions of Ryugu, as well as a few other asteroid candidates for a sample return space mission. Under the assumptions described in their paper, considered as a worse case scenario, they found that sub-surface materials at a depth of only 3–5 cm are much more protected from high temperature than the surface and that they should thus be unaltered at this depth at least from a Sun-driven heating point of view. Thus, their study indicates that it is very likely that a sample collected from Ryugu will be thermally unaltered as long as some of it comes from only 3 to 5 cm depth. Therefore, it is even more likely that material excavated from 1 m, as expected from the SCI, will be unaltered.

4.4 Dust Composed of Low Velocity Ejecta

Although the escape velocity of Ryugu is as small as several 10 cm/s, materials ejected at less than the escape velocity would gradually fall down toward the asteroid in several hours (here we call such ejected materials ‘dust’). The dust slowly returning toward the asteroid with the low velocities might be directly observed by DCAM3-D. The trajectories of the dust with various ejection velocities are shown in Fig. 14, assuming that the scaling law for the ejecta velocity distribution is for a typical sand, $\mu = 0.41$ and $C_1 = 0.55$, and the ejection angle is 45° . In addition, just for simplicity, we ignore the spin of the asteroid and the solar radiation pressure. In Fig. 14, the isochrones of the moving dust corresponding to the dispersed ejecta curtain are also shown by the dotted lines at the time after the impact up to 20 hours. The trajectory of DCAM3-D during the observation will be within 1000 m from the impact point and it will survive for more than 2 hours (Ogawa et al. 2016, in this issue). The ejecta curtain will pass through DCAM3-D and the dust constituting the curtain might hit it within 2 hours. Based on the numerical calculation for the dust trajectories, we can determine the ejection angle and the ejection velocity of the dust, in particular of relatively large dust particles not affected by the solar radiation pressure, passing through or hitting on DCAM3-D. This information on dust could support the scaling law for the velocity distribution constructed from the observation of the ejecta curtain just after the SCI impact.

4.5 Disruption of Boulders

As mentioned in Sect. 2.2, blocks or boulders may exist on the surface of Ryugu. Even though we plan to shoot the SCI projectile toward the possibly existing smooth, sandy surface on Ryugu, there is a possibility that the SCI projectile hits boulders because the predicted impact point of SCI distributes in a wide region with a radius of 200 m (Saiki et al.

2016, in this issue). If the SCI hits a boulder and fragments it into smaller pieces, the resulting data cannot inform us on the cratering process as no crater is really produced, but rather provide us crucial information in another scientific theme: the impact strength and the size distribution of impact fragments of real asteroid materials. The mechanical strength involved in impacts is one of the most important parameters in models of collisional evolution of celestial bodies. The outcome of impact disruption is often measured as a function of the ratio of the kinetic energy of the impactor to the mass of the impacted body, which defines, the specific impact energy or so-called Q . The threshold value of Q , causing that the largest remnant to be one-half the mass of the target, is denoted by Q^* , and there are several models giving different Q^* of celestial bodies based on laboratory impact experiments on the Earth or numerical simulations (e.g., Holsapple et al. 2002). If the SCI hits a boulder on Ryugu, by measuring the resulting fragment's sizes, we can then constrain the Q^* of real asteroid materials. To measure such fragment properties, we should take images of the predicted area of Ryugu to be impacted both before and after the SCI impact with a resolution as high as possible so that we can compare them and distinguish the fragments.

4.6 Seismic Shaking Induced by the SCI Impact

Seismic shaking was firstly determined to be necessary in order to explain observation of small flat-floored craters in the lunar regolith (e.g., Schultz and Gault 1975). Space missions to asteroids (either flybys or rendezvous) provided us close-up images of asteroid surfaces and clarified that mass motion such as slumps and debris aprons frequently occurs (Veverka et al. 2001b). Moreover, the crater size frequency distribution on the small asteroids was found to show a deficiency in the number of small craters (Robinson et al. 2002, Michel et al. 2009), and this deficiency was theoretically studied by Richardson et al. (2005). They proposed that a seismic shaking is the most plausible mechanism to erase small craters and consequently changes the crater size frequency distribution from the one expected by the impact flux on the asteroid surface over time. In their model, the seismic shaking occurs simultaneously when the impact crater is formed by a high-velocity impact of a small body, that is, the strong seismic wave is generated during the cratering process and expands to decay through the asteroid's interior. It was observed in laboratory that the acceleration of seismic waves on a surface of regolith layer is activated by a high-velocity impact (McGarr et al. 1969; Yasui et al. 2015) and the impact induced seismic wave propagates through the regolith layer far from the crater rim. Therefore, we speculate that such a seismic wave in Ryugu may destabilize the material deposited on the steep slopes of the crater inner wall, which could eventually fill partially or totally craters of small enough size, leading to their erasure. Then, naturally the SCI impact is supposed to induce some seismic shaking around the impact crater, and it will be possible for us to evaluate the effect of seismic shaking on Ryugu by means of the observation of the asteroid surface before and after the SCI impact, which will allow us to verify the efficiency of surface motion by this process. We suppose that the area where the seismic shaking occurs depends on the subsurface structure and the physical properties of the constituting materials; so it might provide us some useful information related to the subsurface properties.

5 Summary

In this paper, we introduced the scientific objectives, the expected results, and the observation plan of the SCI impact. Based on the concept described here, we prepared for the SCI operation to maximize its scientific results, and our study is summarized as follows.

- (1) The surface geology of Ryugu is firstly classified according to the size of regolith constituents constructing the surface layer, then the constituent size is compared to the SCI impactor size of 10–20 cm. In total, 7 types of surface structure are possible on Ryugu. Once we succeed in constructing the scaling laws regarding the crater size and the ejecta properties on the asteroid surface, we can apply them to various other important problems concerning celestial body impacts, such as the crater chronology and the erosion and gardening effect on asteroids.
- (2) In addition to the SCI impact crater observed by the onboard cameras, we can use the small crater formed by the sampler projectile to construct the scaling law for the crater size; in particular the crater scaling law of Eq. (1) can be obtained as shown in Fig. 4. Moreover, the scientific purpose of the ejecta curtain observation by DCAM3-D is to determine the scaling law for the ejecta velocity distribution on Ryugu. Then, according to the Z model together with the scaling law for the velocity distribution, we calculate the thickness of the deposits changing with the distance from the edge of the crater when formed in the gravity regime. Furthermore, we estimate the ratio of the constituting materials excavated from different depths, provided that the ejecta layer is so mixed that the order of stratification at deposition cannot be preserved at all.
- (3) If the SCI hits a boulder of Ryugu instead of a granular surface region, we can measure the resulting fragment properties, which would lead to estimate the specific impact energy threshold for disruption, Q_{D^*} , of real asteroid materials.
- (4) The SCI impact may induce seismic shaking around the impact crater, and it is possible for us to evaluate for the first time the effect of seismic shaking on Ryugu by means of the observation of the asteroid surface before and after the SCI impact.

Acknowledgements We are grateful to anonymous referees for many useful suggestions and corrections that helped us to improve this paper. We thank Mr. S. Nakatsubo of the Contribution Division of the Institute of Low Temperature Science, Hokkaido University, and Mr. K. Sengen of Kobe University for their technical help, and we also thank Dr. A.M. Nakamura and Dr. S. Watanabe for their fruitful discussions. We appreciate the help with experiments provided by Dr. Sunao Hasegawa of the Institute of Space and Astronautical Science, JAXA. This work was supported in part by a Grant for a Joint Research Program from the Space Plasma Laboratory, ISAS, JAXA, and was also supported in part by Grants-in-Aid for Scientific Research (23103004, 25610135 and 15K05273) from the Japan Ministry of Education, Culture, Sports, Science and Technology P.M. acknowledges support from the French space agency CNES.

Appendix A: Derivation of Eq. (6)

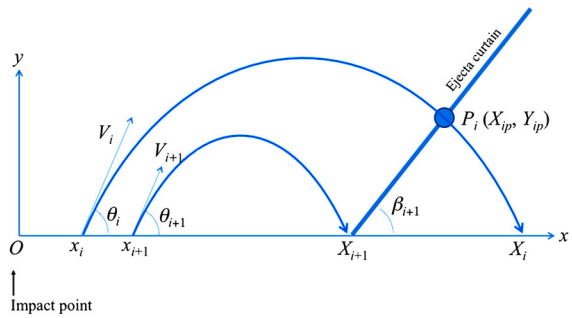
As shown in Fig. 15, which shows a snapshot of the cross section of an ejecta curtain and the ballistic trajectories of ejecta particles composing the curtain, we consider that an ejecta particle P_i ($i = 1, 2, \dots$) originally located on the target surface at a distance x_i from the impact point (here we define $x_i < x_{i+1}$) is ejected at an angle θ_i measured from horizon and a speed V_i . Given that the ejection time of the ejecta particles is 0 and that ejecta particles land at a distance X_i at time t_i under the gravity g , the equations of ballistic motion give

$$X_i = x_i + V_i \cos \theta_i t_i, \quad (7)$$

$$-\frac{1}{2} g t_i^2 + V_i \sin \theta_i t_i = 0. \quad (8)$$

In impact cratering, it is natural to assume $X_i > X_{i+1}$ and $t_i > t_{i+1}$ for $x_i < x_{i+1}$. At time t_{i+1} , the particle P_{i+1} has just landed while the particle P_i has not yet landed (let its position be (X_{ip}, Y_{ip}) in xy -plane) and the base of the ejecta curtain is located at X_{i+1} . At this moment,

Fig. 15 Cross section of ejecta curtain in the xy -plane, showing parameters related to the ejecta curtain



the angle β_{i+1} of the ejecta curtain is given by the angle between the segment $P_i P_{i+1}$ and x -axis and thus

$$\tan \beta_{i+1} = \frac{Y_{ip}}{X_{ip} - X_{i+1}}. \tag{9}$$

From Eqs. (7) and (8), X_{ip} and Y_{ip} are given by

$$X_{ip} = X_i - \frac{gt_i}{2 \tan \theta_i} (t_i - t_{i+1}), \tag{10}$$

$$Y_{ip} = \frac{gt_{i+1}}{2} (t_i - t_{i+1}). \tag{11}$$

Substituting (10) and (11) into (9), we have

$$\frac{t_i}{\tan \theta_i} + \frac{t_{i+1}}{\tan \beta_{i+1}} = \frac{2\Delta X_i}{g\Delta t_i}, \tag{12}$$

where $\Delta X_i = X_i - X_{i+1}$ and $\Delta t_i = t_i - t_{i+1}$. Here let $\Delta t_i \rightarrow 0$, then $t_i \rightarrow t_{i+1} = t$, $\beta_i \rightarrow \beta_{i+1} = \beta$, $\theta_i \rightarrow \theta_{i+1} = \theta$, $\Delta X_i/\Delta t_i \rightarrow dX/dt = \dot{X}$, and (12) becomes

$$\frac{1}{\tan \theta} + \frac{1}{\tan \beta} = \frac{2\dot{X}}{gt}. \tag{13}$$

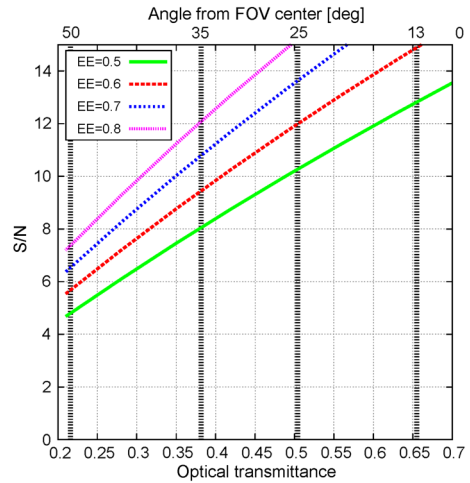
This is Eq. (6) in the text, relating the ejection angle θ and the ejecta curtain angle β using observable parameters: the horizontal proceeding speed \dot{X} of the ejecta curtain, the time t from the moment of impact, and the gravity g .

In the above derivation of Eq. (13), we implicitly assume that the parameters related to the ejecta curtain are observed at the target surface. We can also consider a more general case in which the parameters are given by the observation at a horizon level of height h . In that case, Eq. (13) is extended as

$$\left(1 + \frac{2h}{gt^2}\right) \frac{1}{\tan \theta} + \left(1 - \frac{2h}{gt^2}\right) \frac{1}{\tan \beta} = \frac{2\dot{X}}{gt}, \tag{14}$$

where the angle β and the proceeding speed \dot{X} of the ejecta curtain are measured at the observation level of height h .

Fig. 16 S/N of SCI image in 4-pixels binning as a function of the total transmittance of DCAM3-D optics. Each line shows S/N for each ensquared energy (EE). The angle from FOV center corresponding to the optical transmittance is also shown in the upper horizontal axis



Appendix B: Estimation of S/N of SCI in DCAM3-D Image

We suppose SCI is approximated by a cylinder of $\phi 30 \text{ cm} \times \text{height} 15 \text{ cm}$, wrapped with Beta-cloth with a diffusive reflectance of $\sim 80 \%$, independent of the light wavelength. We consider that the lateral surface of SCI is a uniform diffuse reflector. The specifications of the optics and the imager of DCAM3-D used in this calculation are as follows (see Ishibashi et al. 2016, in this issue, for detail). The spatial resolution is 1 m/pixel , the exposure time is 0.5 msec , the range of the wavelength transmitted through the optics is $450\text{--}700 \text{ nm}$, and the read-out noise of the imager is 7 electron/pixel . The parameters fixed in this calculation are the solar distance of 1.25 AU and the phase angle of the Earth-SCI-Sun of 20 degrees . Then, the free parameters we consider are the transmittance of optics that varies with the angle from the center of FOV, i.e., the position of SCI in an image, and the ensquared energy within 4 pixels. The calculated S/N of SCI image is shown in Fig. 16, in which 4-pixels binning is adopted. Note that the reflectance of SCI surface is assumed to be 50% , not 80% , taking into account that the full surface of SCI is not covered by Beta-cloth. Figure 16 shows that $S/N > 5$ is realized even if the ensquared energy is only 50% and the transmittance of optics is 22% which corresponds to the angle from the FOV center of 50 degrees , i.e., near the corner of a DCAM3-D image.

References

- M.F. A'Hearn et al., Deep impact: excavating comet Tempel 1. *Science* **310**, 258 (2005)
- W.F. Bottke, D.D. Durda, D. Nesvorný, R. Jedicke, A. Morbidelli, D. Vokrouhlický, H. Levison, The fossilized size distribution of the main asteroid belt. *Icarus* **175**, 111 (2005)
- D.T. Britt, D. Yeomans, K. Housen, G. Consolmagno, Asteroid density, porosity, and structure, in *Asteroids III* (2002), p. 485
- A. Colaprete et al., Detection of water in the LCROSS ejecta plume. *Science* **330**, 463 (2010)
- S.K. Croft, Cratering flow fields - implications for the excavation and transient expansion stages of crater formation, in *Lunar and Planetary Science Conference Proceedings*, vol. 11 (1980), p. 2347
- A. Fujiwara et al., The rubble-pile asteroid Itokawa as observed by Hayabusa. *Science* **312**, 1330 (2006)
- D.E. Gault, J.A. Wedekind, Experimental studies of oblique impact, in *Lunar and Planetary Science Conference Proceedings*, vol. 9 (1978), p. 3843
- B. Hapke, *Theory of Reflectance and Emittance Spectroscopy*, 2nd edn. (Cambridge University Press, Cambridge, 2012)

- C.E. Helfrich, A.S. Konopliv, J.V. McAdams, J.K. Miller, W.M. Owen Jr., D.J. Scheeres, S.P. Synnott, B.G. Williams, Estimating the mass of asteroid 253 Mathilde from tracking data during the NEAR flyby. *Science* **278**, 2106 (1997)
- B. Hermalyn, P.H. Schultz, Time-resolved studies of hypervelocity vertical impacts into porous particulate targets: effects of projectile density on early-time coupling and crater growth. *Icarus* **216**, 269 (2011)
- K.A. Holsapple, K.R. Housen, A crater and its ejecta: an interpretation of Deep Impact. *Icarus* **187**, 345 (2007)
- K.A. Holsapple, I. Giblin, K.R. Housen, A. Nakamura, E. Ryan, Asteroid impacts: laboratory experiments and scaling laws, in *Asteroids III*, vol. 443 (2002)
- K.R. Housen, K.A. Holsapple, Ejecta from impact craters. *Icarus* **211**, 856 (2011)
- K.R. Housen, K.A. Holsapple, M.E. Voss, Compaction as the origin of the unusual craters on the asteroid Mathilde. *Nature* **402**, 155 (1999)
- K. Ishibashi, K. Shirai, K. Wada, K. Ogawa, R. Honda, M. Arakawa, N. Sakatani, Y. Ikeda, Optical Performance of Hayabusa2 DCAM3-D camera for short-range imaging of SCI and ejecta. curtain generated from the artificial impact crater formed on Ryugu (2016, accepted)
- M. Ishiguro et al., Optical properties of (162173) Ryugu: in preparation for the JAXA Hayabusa2 sample return mission. *Astrophys. J.* **792**, 74 (2014)
- M. Jutzi, P. Michel, W. Benz, D.C. Richardson, Fragment properties at the catastrophic disruption threshold: the effect of the parent body's internal structure. *Icarus* **207**, 54 (2010)
- M. Kiuchi, A.M. Nakamura, Relationship between regolith particle size and porosity on small bodies. *Icarus* **239**, 291 (2014)
- J.-Y. Li, M.F. A'Hearn, T.L. Farnham, L.A. McFadden, Photometric analysis of the nucleus of Comet 81P/Wild 2 from Stardust images. *Icarus* **204**, 209 (2009)
- D.E. Maxwell, Simple Z model for cratering, ejection, and the overturned flap, in *Impact and Explosion Cratering (Planetary and Terrestrial Implications)* (1977), pp. 1003–1008
- A. McGarr, G.V. Latham, D.E. Gault, Meteoroid impacts as sources of seismicity on the Moon. *J. Geophys. Res.* **74**, 5981 (1969)
- P. Michel, M. Delbo, Orbital and thermal evolutions of four potential targets for a sample return space mission to a primitive near-Earth asteroid. *Icarus* **209**, 520 (2010)
- P. Michel, W. Benz, P. Tanga, D.C. Richardson, Collision and gravitational reaccumulation: forming asteroid families and satellites. *Science* **294**, 1696 (2001)
- P. Michel, D.P. O'Brien, S. Abe, N. Hirata, Itokawa's cratering record as observed by Hayabusa: implications for its age and collisional history. *Icarus* **200**, 503 (2009)
- J.K. Miller, A.S. Konopliv, P.G. Antreasian, J.J. Bordi, S. Chesley, C.E. Helfrich, W.M. Owen, T.C. Wang, B.G. Williams, D.K. Yeomans, D.J. Scheeres, Determination of shape, gravity, and rotational state of asteroid 433 Eros. *Icarus* **155**, 3 (2002)
- K. Ogawa, K. Shirai, H. Sawada, M. Arakawa, K. Wada, R. Honda, K. Ishibashi, N. Sakatani, S. Nakazawa, H. Hayakawa, System configuration and operation plan of Hayabusa2. DCAM3-D for scientific observation in SCI impact experiment. *Space Sci. Rev.* (2016, accepted)
- J.E. Richardson, H.J. Melosh, An examination of the Deep Impact collision site on Comet Tempel 1 via Stardust-NExT: placing further constraints on cometary surface properties. *Icarus* **222**, 492 (2013)
- J.E. Richardson Jr., H.J. Melosh, R.J. Greenberg, D.P. O'Brien, The global effects of impact-induced seismic activity on fractured asteroid morphology. *Icarus* **179**, 325 (2005)
- J.E. Richardson, H.J. Melosh, C.M. Lisse, B. Carcich, A ballistics analysis of the Deep Impact ejecta plume: determining Comet Tempel 1's gravity, mass, and density. *Icarus* **191**, 176 (2007)
- M.S. Robinson, P.C. Thomas, J. Veveřka, S.L. Murchie, B.B. Wilcox, The geology of 433 Eros. *Meteorit. Planet. Sci.* **37**, 1651 (2002)
- T. Saiki, H. Imamura, M. Arakawa, K. Wada, Y. Takagi, M. Hayakawa, K. Shirai, H. Yano, C. Okamoto. Small Carry-on Impactor (SCI) for Hayabusa2 Impact Experiment. *Space Sci. Rev.* (2016, accepted). [10.1007/s11214-016-0297-5](https://doi.org/10.1007/s11214-016-0297-5)
- D.J. Scheeres, C.M. Hartzell, P. Sánchez, M. Swift, Scaling forces to asteroid surfaces: The role of cohesion. *Icarus* **210**, 968 (2010)
- P.H. Schultz, D.E. Gault, Seismically induced modification of lunar surface features, in *Lunar and Planetary Science Conference Proceedings*, vol. 6 (1975), p. 2845
- P.H. Schultz, D.E. Gault, Clustered impacts: experiments and implications. *J. Geophys. Res., Solid Earth* **90**, 3701 (1985)
- P.H. Schultz, C.M. Ernst, J.L. Anderson, Expectations for crater size and photometric evolution from the Deep Impact collision, in *Deep Impact Mission: Looking Beneath the Surface of a Cometary Nucleus* (2005), p. 207
- P.H. Schultz, C.A. Eberhardy, C.M. Ernst, M.F. A'Hearn, J.M. Sunshine, C.M. Lisse, The Deep Impact oblique impact cratering experiment. *Icarus* **191**, 84 (2007)

- P.H. Schultz, B. Hermalyn, A. Colaprete, K. Ennico, M. Shirley, W.S. Marshall, The LCROSS cratering experiment. *Science* **330**, 468 (2010)
- P.H. Schultz, B. Hermalyn, J. Veveřka, The Deep Impact crater on 9P/Tempel-1 from Stardust-NExT. *Icarus* **222**, 502 (2012)
- P. Shalima, K. Wada, H. Kimura, Ejecta curtain radiative transfer modeling for probing its geometry and dust optical properties. *Planet. Space Sci.* **116**, 39–47 (2015)
- S. Tachibana et al., Hayabusa2: Scientific importance of samples returned from C-type near-Earth asteroid (162173) Ryugu. *Geochem. J.* **48**, 571 (2014)
- Y. Takagi, S. Hasegawa, H. Yano, S. Syamamoto, S. Sugita, K. Teramoto, C. Honda, K. Kurosawa, T. Nakada, M. Abe, A. Fujiwara, Impact cratering experiments in microgravity environment, in *Proc. Lunar Planet. Sci. XXXVIII* (2007), p. 1634
- Y. Tsuda, M. Yoshikawa, M. Abe, H. Minamino, S. Nakazawa, System design of the Hayabusa2—asteroid sample return mission to Ryugu. *Acta Astronaut.* **91**, 356 (2013)
- S. Tsujido, M. Arakawa, K. Wada, A.I. Suzuki, Experimental study on the ejecta velocity distribution during the crater formation and implication for Wada's method, in *2013 Fall Meeting of Japanese Planetary Science Society. Proceedings of the Conference* (2013) (in Japanese)
- S. Tsujido, M. Arakawa, A.I. Suzuki, M. Yasui, Ejecta velocity distribution of impact craters formed on quartz sand: effect of projectile density on crater scaling law. *Icarus* **262**, 79 (2015)
- J. Veveřka et al., Imaging of small-scale features on 433 Eros from NEAR: evidence for a complex regolith. *Science* **292**, 484 (2001a)
- J. Veveřka et al., The landing of the NEAR-shoemaker spacecraft on asteroid 433 Eros. *Nature* **413**, 390 (2001b)
- K. Wada et al., Large scale impact experiments simulating Small Carry-on Impactor (SCI) equipped on Hayabusa2, in *Lunar and Planetary Science Conference*, vol. 45 (2014), p. 1768
- M. Yasui, M. Arakawa, Compaction experiments on ice-silica particle mixtures: implication for residual porosity of small icy bodies. *J. Geophys. Res., Planets* **114**, E09004 (2009)
- M. Yasui et al., In situ flash X-ray observation of projectile penetration processes and crater cavity growth in porous gypsum target analogous to low-density asteroids. *Icarus* **221**, 646 (2012)
- M. Yasui, E. Matsumoto, M. Arakawa, Experimental study on impact-induced seismic wave propagation through granular materials. *Icarus* **260**, 320–331 (2015)
- D.K. Yeomans et al., Estimating the mass of asteroid 253 Mathilde from tracking data during the NEAR flyby. *Science* **278**, 2106 (1997)